Nano Research

Open Access

Research Article

Highly portable electrochemical oxygen removal device for microenvironmental low-oxygen control

Xin Wang[1], Xingen Lin[1], Wanyu Shen[1], Yimin Li[1], Yi Tan[1], Zihan Wang[1], Peng Jiang[1], Song Gong[3] ✉, Kong Chen[1,2] ✉, Yu Zhang[1,2] ✉, and Yuen Wu[1,2] ✉

[1] *Department of Endocrinology, Institute of Endocrine and Metabolic Diseases, The First Affiliated Hospital of University of Science and Technology of China (USTC), Division of Life Sciences and Medicine, University of Science and Technology of China, Hefei 230001, China*
[2] *Deep Space Exploration Laboratory, University of Science and Technology of China, Hefei 230026, China*
[3] *Division of Endocrinology, Tongji Hospital, Huazhong University of Science and Technology, Wuhan 430030, China*

Cite this article: *Nano Research*, **2025**, *18*, 94907179. https://doi.org/10.26599/NR.2025.94907179

ABSTRACT: Low-oxygen (O_2) environments are essential in various research and application fields, yet traditional methods like nitrogen flushing or chemical O_2 absorbers face challenges in high equipment cost and low controllability. This study introduces a novel electrochemical oxygen removal (EOR) controller, offering a lightweight, low-cost, and precise low-O_2 control solution. The self-powered EOR controller uses a sacrificial anode to drive the cathodic oxygen reduction reaction (ORR), efficiently consuming environmental O_2 to reduce its level, thus eliminating the requirements of external gas or power sources. By integrating a single-atom ORR catalyst and flexible design, the device achieves a substantial reduction in weight and cost. The incorporation of electronic components for the EOR controller, including a switch for reaching targeted O_2 concentration and a fixed resistor for O_2 removal rate regulation, enables multi-dimensional O_2 removal control. The system also realizes the O_2 concentration estimation in real-time with ±1% accuracy (within the 21%–1% range) by calculating electron transfers. The EOR controller's effectiveness is validated in plant hypoxia stress experiments, demonstrating precise O_2 level adjustments and its potential across various applications requiring controlled hypoxic conditions.

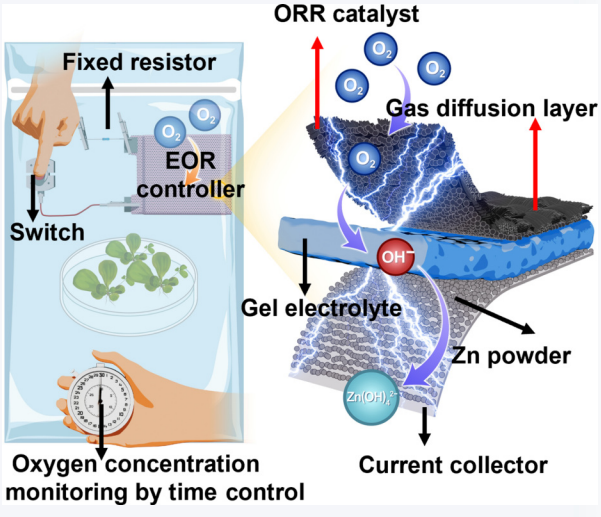

KEYWORDS: low-oxygen condition, oxygen reduction reaction (ORR), oxygen level control for microenvironment, electrochemical oxygen removal

1 Instructions

Hypoxic conditions and precise control over varying oxygen (O_2) concentrations are crucial in fields such as biomedicine, genomics, molecular biology, synthetic biology, fruit preservation and anaerobic fermentation [1–4]. For instance, the primary tumor area often experiences hypoxia, so simulating an environment with different low-O_2 concentrations can replicate the tumor microenvironment, allowing the study of its impact on tumor cell metabolism, proliferation, and drug resistance [5, 6]. In plant science, controlling low-O_2 levels is vital for studying the adaptive mechanism of plants under hypoxic surroundings, such as inhibition of seed germination, anaerobic respiration, and internodal elongation [7–9]. In microbiology and fermentation, the precise control of specific low-O_2 concentrations is a key factor in optimizing anaerobic or microaerophilic microbial fermentation, as well as improving yield and product quality [10–12]. Given the importance of creating and controlling hypoxic conditions across various fields, it is essential to develop an O_2 removal device that offers convenient, controllable, and precise O_2 removal capabilities.

Traditional strategies for creating low-O_2 environments primarily involve high-purity nitrogen (N_2) flushing and

Received: October 29, 2024; **Revised:** December 10, 2024
Accepted: December 10, 2024

✉Address correspondence to Song Gong, gongsong@tjh.tjmu.edu.cn; Kong Chen, kongchen@ustc.edu.cn; Yu Zhang, zy11260@ustc.edu.cn; Yuen Wu, yuenwu@ustc.edu.cn

spontaneous chemical reactions for O_2 absorption [13–15]. The N_2 flushing strategy requires the integration use of multiple equipment systems, including N_2 production equipment, gas pipeline and control devices, which significantly increases the complexity and cost of the setup (Fig. 1(a)). The O_2 absorption strategy works through the spontaneous chemical reaction of internal active materials with O_2, thereby reducing the O_2 concentration in the environment (Fig. 1(b)). However, this method completely lacks control over the O_2 removal process, limiting its use in applications that require precise adjustments of O_2 concentration. Therefore, there is a critical need to develop a new O_2 removal technology that addresses the shortcomings of traditional strategies, enabling lightweight, convenient, and highly controllable O_2 removal.

The drawbacks of traditional O_2 removal strategies primarily stem from their O_2 removal mechanisms. N_2 flushing always requires N_2 generation and gas control equipment (such as N_2 cylinders, pressure swing adsorption (PSA) generators, and gas controllers), which fundamentally limits the miniaturization of the system. O_2 absorption rely on spontaneous chemical reactions, making it difficult to achieve precise control over the O_2 removal process. In contrast, electrochemical strategy may offer a more efficient approach. The electrocatalytic oxygen reduction reaction (ORR) involves converting O_2 from the air into water or oxygen-containing intermediate ions [16–21], thereby directly removing O_2 from the environment and eliminating the reliance on a N_2 source, facilitating the lightweight design of the device. Moreover, unlike spontaneous chemical reactions, the electrochemical process can be precisely controlled by adjusting electrical parameters, allowing for multi-dimensional control of the O_2 removal process. For instance, the applying or cutoff of the power supply directly governs the initiation and termination of the electrochemical reaction. Besides, the current in the electrochemical system indicates the electron transfer rate between the cathode and the anode. Thus, directly adjusting its magnitude precisely regulates the rate of the electrochemical reaction. In addition, the number of electron transfers during the reaction period determines the consumption and generation amounts of reactants and products, thereby directly influencing their final concentrations. Therefore, adopting an electrochemical strategy may fundamentally overcome the limitations of traditional methods, making it a promising technology for efficient and controllable O_2 removal. In ORR catalysts, platinum-based materials exhibit excellent catalytic activity; however, their high cost and scarcity have driven the pursuit of alternatives. Emerging single-atom catalysts have attracted significant attention due to their cost-effectiveness and promising activity [22–26].

In this study, a novel O_2 removal device based on electrochemical principles was developed, specifically designed for efficient and precise low-O_2 control. This self-powered electrochemical oxygen removal (EOR) device utilizes a sacrificial anode to drive the cathodic ORR, efficiently consuming O_2 and thus reducing the environmental O_2 level. Such design eliminates the need for an external gas source and power supply, enabling the miniaturization of the device (Fig. 1(c)). By developing a single-atom ORR catalyst and incorporating a flexible structure into the EOR, the cost and weight of the device were significantly reduced, enhancing its cost-efficiency and portability. The control of the O_2 removal process in the EOR can be conveniently achieved by integrating electronic components into the system. This includes using a switch for real-time start–stop control of the EOR system,

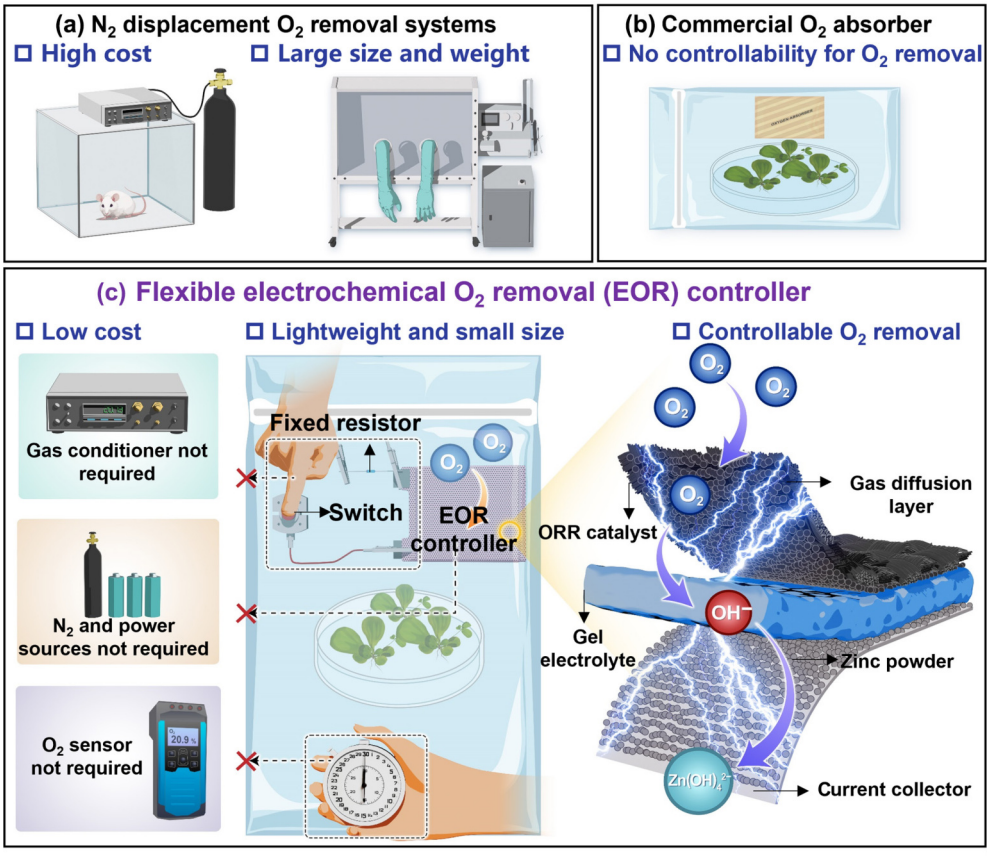

Figure 1 Comparison of different O_2 removal strategies: (a) N_2 flushing, (b) chemical O_2 absorption, and (c) electrochemical O_2 removal.

allowing for targeted O_2 concentration control, and employing fixed resistors to adjust currents of the system, providing convenient regulation of the O_2 removal rates. Additionally, this study demonstrated that the EOR system can accurately estimate environmental O_2 concentrations in real-time by calculating the number of electron transfers during the O_2 removal process, with a margin of error less than ±1% (for concentrations ranging from 21% to 1%). This result suggests that the EOR can eliminate the need for traditional O_2 concentration sensors, further enhancing its functional diversity. The developed EOR controller effectively regulated O_2 levels in plant hypoxia stress experiments, replacing the need for O_2 concentration sensors by accurately estimating and adjusting O_2 levels of experimental environment. In summary, the study presents a highly efficient, portable, and cost-effective solution for controllable O_2 removal, which holds significant potential for future applications in fields requiring low-O_2 environments.

2 Experimental

2.1 Materials

All the reagents were directly used without purification. Carbon black (CB, XC-72) was purchased from Suzhou Sinero Technology Co., Ltd. Iron(III) nitrate nonahydrate ($Fe(NO_3)_3{\cdot}9H_2O$), cobalt(II) nitrate hexahydrate ($Co(NO_3)_2{\cdot}6H_2O$), dicyanodiamide ($C_2H_4N_4$, 98%), acrylamide (AM, C_3H_5NO, 98%), acrylic acid (AA, $C_3H_4O_2$, 99%), N,N'-methylenebisacrylamide (MBA, $C_7H_{10}N_2O_2$), ammonium persulfate ($(NH_4)_2S_2O_8$, 98%), potassium hydroxide (KOH, 85%), O-phenanthroline monohydrate ($C_{12}H_8N_2{\cdot}H_2O$), sulfuric acid (H_2SO_4, 95%–98%), zinc powder (Zn, 95%), MnO_2 and Co_3O_4 were purchased from Sinopharm Chemical Reagent Co., Ltd. Methanol (CH_3OH) and ethyl alcohol (95%) were purchased from Shanghai Titan Scientific Co., Ltd.

2.2 Preparation of catalyst

Typically, 5 g carbon black (XC-72) was added to a glassy chromatography column, and then O_3 was injected into the glass column at a rate of 1.0 L·min^{-1} for 8 h continuously with an O_3 concentration of 60 mg·L^{-1}. After the reaction, the product was collected and labeled as O-C. Then, 500 mg of O-C is added to a beaker containing 50 mL of anhydrous ethanol and dispersed by ultrasonic treatment to form a dispersion. Then 36.4 mg $Fe(NO_3)_3{\cdot}9H_2O$ was dissolved in 20 mL anhydrous ethanol as a solution. At room temperature, the solution was pumped into the strongly stirred carbon black dispersion with a micro-injection pump at the rate of 0.5 mL·min^{-1}. After stirring for 1 h, 71.4 mg of 1,10-phenanthroline in ethanol solution was added. After the solution was completely added, the solution was continuously stirred for 7 h. The catalyst precursor was transferred to a 90 °C constant temperature oil bath and stirred until the anhydrous ethanol evaporated. The obtained catalyst precursor was mixed with dicyandiamide according to the mass ratio of 1:5, and the uniform mixture was obtained by ball milling for 2 h. In Ar atmosphere, heating at 900 °C for 2 h, the heating rate is 5 °C·min^{-1}. Finally, the particles were removed by pickling to form Fe-N-C. The preparation method of Co-N-C is the same as that of Fe-N-C, except that $Fe(NO_3)_3{\cdot}9H_2O$ is replaced with $Co(NO_3)_2{\cdot}6H_2O$.

2.3 Preparation of the hydrogel electrolyte

The hydrogel electrolyte was prepared by a simple one-pot method. Mix 10 g AM powder with 10 mL AA in a beaker, then add deionized water to 50 mL, then add 7 mg MBA and stir vigorously at room temperature until the powder is completely dissolved. N_2 is then passed into the beaker and air is vented for 15 min. Ammonium persulfate is then added (0.1 g ammonium persulfate is dissolved in 1 mL deionized water). After stirring for another 30 s, transfer the mixture to a petri dish and seal it with plastic wrap. Polymerized at 70 °C for 2 h, then took off the plastic wrap and continued drying for 4 h to obtain polyacrylamide-polyacrylic acid (PAM-PAA) gel electrolyte. Before the experiment, the gel electrolyte was soaked in 6 M KOH solution for at least 6 h.

2.4 Assembly of flexible electrochemical oxygen removal reactor

Weigh a certain amount of the catalyst and add it to a mixed solution of isopropanol and water in a volume ratio of 7:3. Then, add a specific amount of Nafion solution. Ultrasonically stir the mixture until homogeneous, then spray it onto carbon cloth with a loading of 1 mg·cm^{-2}, which will serve as the air cathode. Add a certain amount of 6 M KOH solution to zinc powder to prepare zinc paste, which is then coated onto a 0.05 mm zinc foil and allowed to air dry naturally to form the anode. Cut PAM-PAA gel, which has been soaked in 6 M KOH solution, into appropriate shapes to serve as the semi-solid electrolyte. Assemble the flexible electrochemical O_2 removal in a mold in the sequence of air cathode, semi-solid electrolyte, and anode.

2.5 Electrochemical measurements

The electrocatalytic ORR performance were evaluated using CHI 760E electrochemical station at room temperature with a conventional three-electrode system. All potentials (E) were measured against an Ag/AgCl reference electrode and corrected to the reversible hydrogen electrode (RHE) scale by the following equation

$$E\,(\text{V vs. RHE}) = E\,(\text{V vs. Ag/AgCl}) + 0.197\ \text{V} + 0.059 \times \text{pH} \quad (1)$$

5 mg of catalyst was dispersed in 1 mL of an ethanol/water mixed solvent, and then added 40 μL of 5 wt.% Nafion solution. The above mixed solution was sonicated for at least 40 min to form a homogeneous ink. For ORR, 10 μL of the catalyst ink was dropped onto a glassy carbon disc (0.1963 cm^2 of disc area) and dried to form a uniform thin film. Before the measurement, a stream of N_2/O_2 flow was delivered to the electrolyte for 30 min to obtain an N_2/O_2-saturated solution. linear sweep voltammetry (LSV) curves were conducted in O_2-saturated 0.1 M KOH at room temperature, and measured at various rotating speed from 625 to 2500 rpm with a sweep rate of 10 mV·s^{-1}. The yielding of H_2O_2 (H_2O_2%) and electron transfer number (n) were calculated according to the following equations

$$H_2O_2\% = 200 \times \frac{\frac{I_R}{N}}{I_d + \frac{I_R}{N}} \quad (2)$$

$$n = 4 \times \frac{I_d}{I_d + \frac{I_R}{N}} \quad (3)$$

In the two equations, I_d is the disk current, I_R is the ring current and N is the current collection efficiency of the Pt ring (N = 0.37).

The kinetic current (J_K) was calculated following the Koutecky–Levich (K–L) equation

$$\frac{1}{J} = \frac{1}{J_L} + \frac{1}{J_K} = \frac{1}{B\omega^{1/2}} + \frac{1}{J_K} \quad (4)$$

$$B = 0.62nFC_0D_0^{2/3}\nu^{-1/6} \quad (5)$$

In the two equations, J_L and J_K represent the diffusion- and kinetic-limiting current density, respectively. ω is the angular velocity. n denotes the number of electrons transferred per O_2, F is the Faraday constant (96,485 C·mol^{-1}). C_0 is the saturated concentration of O_2 in 0.1 M KOH solution (1.2×10^{-6} mol·cm^{-3}). D_0 is the diffusion coefficient of O_2 in 0.1 M KOH electrolyte (1.9×10^{-5} cm^2·s^{-1}). ν is the kinetic viscosity of the electrolyte (0.01 cm^2·s^{-1}).

2.6 Calculation of O_2 removal amount

Calculation of O_2 removal amount at constant voltage

$$O_2\text{-removal (L)} = V_0 - V_t = V_0x_0 - V_tx_t \quad (6)$$

$$V_t = \frac{V_0(1-x_0)}{1-x_t} \quad (7)$$

In the above two equations, V_0 is the initial volume (L), and V_t is the volume after O_2 removal (L). x_0 is the initial oxygen concentration (20.9%), and x_t is the oxygen concentration after O_2 removal.

Calculation of O_2 removal amount based on charge transfer

$$O_2\text{-removal (L)} = \frac{I \times t}{4F} \times V_m \quad (8)$$

In the equation, I (A) is electric current during O_2 removal process, t is the O_2 removal time (s), and V_m is the molar volume at 25 °C (24.5 L·mol^{-1}).

2.7 Characterization

Transmission electron microscopy (TEM) measurement was carried out on Hitachi-7700 microscopy with an acceleration voltage of 100 kV. High-resolution TEM (HRTEM), high-angle annular dark-field scanning TEM (HAADF-STEM), and energy-dispersive X-ray spectroscopy (EDS) elemental mapping were implemented on a JEM-2100F microscopy. The aberration-corrected HAADF-STEM was taken on Titan Cubed Themis G2 300. Powder X-ray diffraction (XRD) patterns of samples were recorded on a Rigaku Miniflex600 operating at 40 kV voltage and 15 mA current with Cu Kα radiation (λ = 0.15406 nm). The measurements of Brunauer–Emmett–Teller (BET) specific surface areas for samples were performed on a Micromeritics Tristar II 3020M to obtained adsorption desorption isotherms, and the samples were degassed at 300 °C for 3 h. Raman spectra were obtained using the Horiba LabRAM HR Evolution Raman spectrometer with a laser excitation of 532 nm. X-ray photoelectron spectroscopy (XPS) spectra were collected by Thermo Scientific ESCALAB 250Xi X-ray photoelectron spectrometer using Al Kα radiation and the C 1s peak at 284.8 eV as an internal standard. Inductively coupled plasma-atomic emission spectrometry (ICP-AES) results were collected by Thermo Fisher iCAP 7400 to analyze the element content of Fe in samples. The X-ray absorption fine structure (XAFS) spectra of Fe K-edge was obtained in 1W1B station of Beijing Synchrotron Radiation Facility (BSRF).

2.8 Plant growth

All *Arabidopsis* plants are in Columbia-0 (Col-0) ecotype background. Plant grew according to the following procedure [27]. Seeds were sterilized with 5% sodium hypochlorite for 15 min. After rinsed 3 times in sterile-deionized water, seeds grown horizontally on the plates containing 1/2 Murashige and Skoog (1/2 MS) (PhytoTech), 0.8% (w/v) agar, 1% sucrose, pH = 5.7. Then the seeds were stratified at 4 °C for 3 days. For anoxic assay, 2-week-old plants were transferred to an airtight bag containing the EOR controller, and then imaged after indicated duration. Seedlings grew in a chamber under a 16 h light/8 h dark photoperiod at 23 °C.

2.9 Laser scanning confocal microscopy

The green fluorescent protein (GFP) fluorescence in the roots of 1-week-old 2.3-GFP seedlings were observed after 4 h treatment by EOR controller at indicated oxygen concentration. GFP fluorescence was visualized with a Zeiss LSM880 inverted confocal scanning microscopy. Excitation wavelength (Ex): 488; emission wavelength (Em): 507.

2.10 Seed germination

Arabidopsis seeds germinated under indicated oxygen concentration adjusted by the EOR controller. After 5 days, the plates were imaged and germination ratios were calculated.

3 Result and discussion

The cathodic ORR is the core process of the EOR controller, consuming O_2 to lower the environmental O_2 levels. To significantly save the cost of the ORR catalyst, an Fe single-atom catalyst based on a carbon material substrate was developed. For the catalyst synthesis, the substrate CB was treated with ozone, and this method successfully introduced a large number of oxygen-containing functional groups on its surface. Raman spectroscopy (Fig. S1 in the Electronic Supplementary Material (ESM)) reveals the increased I_D/I_G value (1.05) of the O-C compared to its untreated counterpart (0.97), indicating an increase in defect sites, and this may facilitate the subsequent adsorption of metal ions. The Fe-N-C single-atom catalyst was synthesized by adsorbing Fe^{2+} ions on O-C through electrostatic interaction and then calcining at high temperature in the presence of a mixed nitrogen source. The actual elemental content was determined by ICP-AES (Table S1 in the ESM), showing a loading of 1.31% for Fe. TEM images (Fig. S2 in the ESM) show the same morphology for CBs before and after Fe loading. BET results (Fig. S3 in the ESM) indicate a large surface area (150.55 m^2·g^{-1}) of Fe-N-C. The successful synthesis of the Fe-N-C single-atom catalyst was confirmed by HRTEM (Fig. S4 in the ESM), HAADF-STEM images (Fig. 2(a)), and XRD (Fig. S5 in the ESM) results. The EDS images also illustrate that Fe atoms are highly dispersed on the carbon support (Fig. S6 in the ESM). Normalized X-ray absorption spectroscopy (XAS) of the Fe K-edge shows that the valence state of Fe is located between Fe foil and Fe_2O_3 (Fig. 2(b)), and the fitting result is +2.83 (Fig. S7 in the ESM). The results of the Fourier transform k^3-weighted extended XAFS (FT-EXAFS) and the wavelet transform (WT) image (Fig. 2(c) and Fig. S8 in the ESM) jointly confirm the absence of Fe–Fe metallic bonds and the predominant Fe–N bonds in Fe-N-C, and fitting results (Table S2 and Fig. S9 in the ESM) indicate that the coordination structure of this Fe-N-C is Fe–N_4. The N 1s spectra in the XPS of Fe-N-C reveals that the nitrogen species in Fe-N-C are

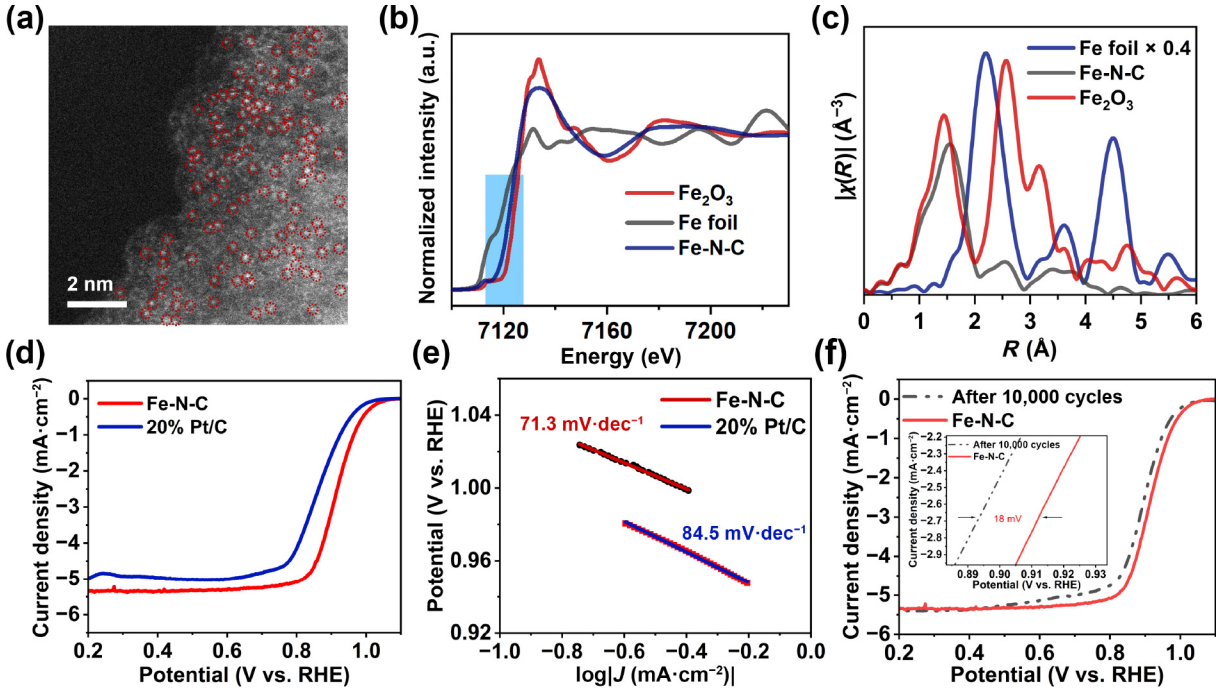

Figure 2 (a) The HAADF-STEM image of Fe-N-C. (b) Normalized XAS of the Fe K-edge. (c) The k^3-weighted FT-EXAFS spectra of Fe for Fe foil, Fe-N-C and Fe_2O_3 at *R* space. (d) The ORR performances of Pt/C and the Fe-N-C evaluated by a RDE in 0.1 M KOH. (e) The Tafel plots for Fe-N-C and Pt/C. (f) Stability measurement for Fe-N-C.

primarily pyrrolic N, pyridinic N, and graphitic N (Fig. S10 in the ESM). The ORR performance of the Fe-N-C catalyst was evaluated using a rotating disk electrode (RDE) in 0.1 M KOH. The results, presented in Fig. 2(d), reveal that the half-wave potential of Fe-N-C is 0.91 V vs. RHE, exceeding that of commercial Pt/C (0.86 V vs. RHE), thereby highlighting its enhanced ORR activity. In contrast, the commercial MnO_2, Co_3O_4, Co-N-C, and N-C exhibit poor ORR activity (Fig. S11 in the ESM), identifying Fe as the active site for ORR. Based on the LSV curve analysis (Fig. S12 in the ESM) conducted within the rotational speed range of 625–2500 rpm, the number of electron transfers of Fe-N-C derived from the K–L equation (Fig. S13 in the ESM) is around 4, indicating that its ORR proceeds through a 4-electron pathway. This result is further confirmed by rotating ring-disk electrode (RRDE) measurements (Fig. S14 in the ESM), which also show an electron transfer number of 4. The Tafel slopes of all catalysts are shown in Fig. 2(e). Fe-N-C shows a Tafel slope of 71.3 mV·dec^{-1} for ORR, superior to the commercial catalyst Pt/C (84.5 mV·dec^{-1}). This indicates excellent kinetics and electron transfer efficiency of ORR for Fe-N-C. Figure 2(f) demonstrates the excellent stability of Fe-N-C, showing minimal degradation after 10,000 ORR cycles. The comparison of XRD patterns before and after the reaction, along with the TEM images after the reaction, also reflect the stability of its atomic dispersion (Figs. S15 and S16 in the ESM).

The core principle of the EOR controller leverages spontaneously generated electromotive force to drive the cathodic ORR, consuming environmental O_2 and thus lowering ambient concentrations. Utilizing a primary cell structure, the EOR controller operates without an external power source. O_2 removal via the ORR mechanism is more efficient and direct, thus eliminating the requirement for N_2 supply equipment. These designs drastically reduce the volume, cost, weight, and complexity of the EOR controller, resulting in an ultra-miniaturized device. The electrochemical reaction mechanism of EOR is depicted in Fig. 3(a). The negative electrode of the EOR is composed of the sacrificial metal zinc, and the positive electrode utilizes a synthesized Fe-N-C ORR catalyst with atmospheric O_2 as the reactant. The reactions at both electrodes occur in an alkaline environment as follows [28]

$$\text{Negative electrode: } Zn + 4OH^- - 2e^- \rightarrow Zn(OH)_4^{2-} \quad (9)$$

$$\text{Positive electrode: } O_2 + 2H_2O + 4e^- \rightarrow 4OH^- \quad (10)$$

The assembly process of the EOR device is illustrated in Fig. 3(b). The process begins by casting silicone gel in a glass mold to form a flexible silicone shell with grooves. The zinc anode, home-made gel separator, ORR catalyst-loaded gas diffusion electrode (GDE) are sequentially assembled and embedded into these grooves. All edges are sealed with silicone gel to enhance airtightness and prevent electrolyte leakage. To prevent the volatilization of alkaline substances during O_2 removal, the surface of the EOR controller is coated with a protective layer of 3 Å molecular sieve, which is then encapsulated by a piece of non-woven fabric. By placing moistened pH paper on the working area of the EOR controller to detect any leakage of alkaline substances, the results demonstrated that the molecular sieve effectively blocked the diffusion of alkaline substances, maintaining a neutral environment on the outside of the EOR (Fig. S17 in the ESM). This flexible design of EOR enables versatile integration into various O_2 removal settings and substantially reduces both weight and component costs. The EOR controller weighs approximately 47.6 g and has dimensions of 8.1 cm × 5.4 cm × 1.0 cm, offering excellent portability (Fig. S18 in the ESM). As shown in Fig. S19 in the ESM, the proper functioning of the EOR controller is verified by a luminescent electronic indicator. During the O_2 removal experiments, the positive and negative electrodes of the EOR were linked directly. Then the EOR controller was placed in an airtight bag filled with 500 mL of air,

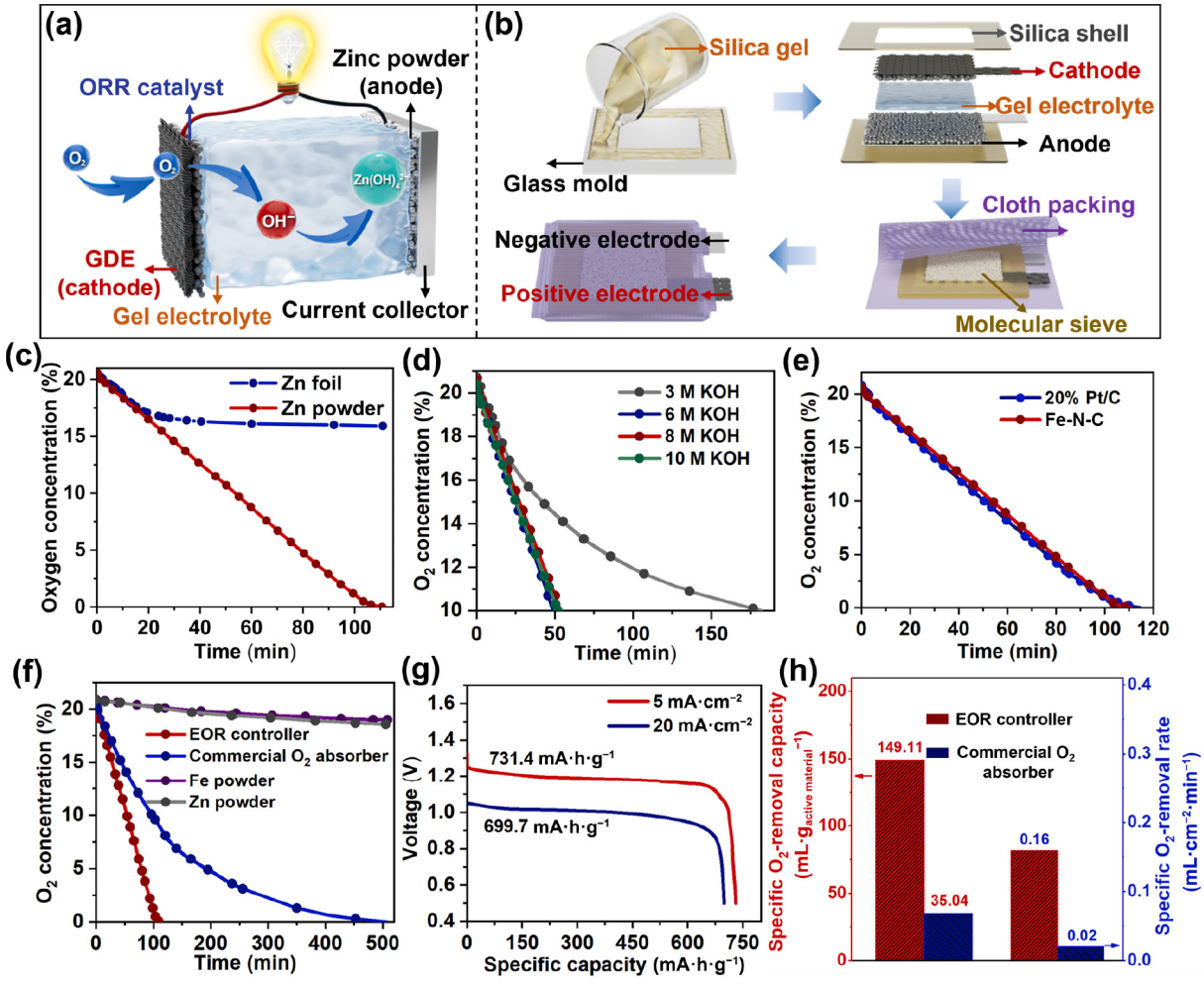

Figure 3 (a) and (b) The reaction mechanism and the fabrication procedures of the EOR controller. (c) and (d) The O_2 removal performances for different positive materials, and different alkaline concentrations of the EOR controller. (e) The O_2 removal comparison for the EOR controllers with Pt/C, or Fe-N-C as the ORR catalyst. (f) The O_2 removal comparison for different O_2 removal materials. (g) The specific discharge capacity of EOR controller at different current densities. (h) The comparison between EOR controller with commercial O_2 absorber for specific O_2 removal capacity and rate.

with O_2 levels monitored by an O_2 concentration sensor under various conditions. Figure 3(c) illustrates the O_2 removal results for different zinc anodes. The direct use of zinc foil as the anode results in a reduction in the O_2 removal rate, halting further O_2 removal when the oxygen concentration reaches 16.4%. The XRD analysis of the zinc foil after the reaction (Fig. S20 in the ESM) reveals the formation of a dense zincite (ZnO) layer on its surface, which blocks contact between the zinc and the electrolyte, thereby reducing zinc utilization. In contrast, using zinc powder as the anode significantly improved zinc utilization due to its larger specific surface area, reducing the environmental O_2 concentration from 21% to 0% within 112 min. Therefore, zinc powder was chosen as the anode material for subsequent experiments. Home-made hydrogels containing KOH solutions with concentrations of 3, 6, 8, and 10 M were used as diaphragm materials in the EOR controller, with O_2 removal performance shown in Fig. 3(d). The results indicate that the O_2 removal rate at a 3 M KOH concentration was significantly lower than that at other higher concentrations. This might be due to the formation of an insoluble zinc hydroxide ($Zn(OH)_2$) layer on the electrode surface during reaction period, causing electrode passivation and inhibiting the reaction activity. In contrast, higher alkaline concentrations (6, 8, and 10 M) of KOH facilitate $Zn(OH)_2$ transforming into soluble zincate ions ($Zn(OH)_4^{2-}$), eliminating such passivation effect and exhibiting similar O_2 removal performance. Hence, 6 M KOH was selected as the standard alkali concentration for subsequent experiments. Figure 3(e) shows that the synthesized Fe-N-C ORR catalyst exhibits a similar O_2 removal performance to that of commercial 20% Pt/C, indicating it can effectively replace the precious metal catalyst to greatly lower the catalyst cost. Figure 3(f) shows a comparison of the O_2 removal conditions of EOR with different chemical O_2 absorbing agents. Zinc and iron powders exhibited weak O_2 consumption activities; while for the commercial O_2 absorber, it is significantly lower than that of EOR with a gradually degraded O_2 removal rate. In stark comparison, the EOR controller not only demonstrated the highest O_2 removal efficiency but also maintained a nearly constant O_2 removal rate throughout. The above results highlight the superiority of the electrically driven ORR O_2 removal mechanism, which provides higher and more stable O_2 consumption efficiency than those traditional spontaneous O_2 consumption reactions. Figure 3(g) presents the specific discharge capacity of EOR controller, recording 731.4 and 699.7 mA·h·g^{-1} at current densities of 5 and 20 mA·cm^{-2}, respectively, with zinc utilization ratios calculated as 89.4% and

85.5%. This result surpasses most reported flexible zinc-air batteries (Table S3 in the ESM), evidencing superior zinc utilization efficiency for the EOR controller. The O_2 removal abilities towards per unit active material mass and per unit active area were measured for both the EOR controller and a commercial O_2 absorber through actual O_2 removal experiments. The EOR controller demonstrated a larger O_2-removal capacity of 149 $mL{\cdot}g_{Zn}^{-1}$ and higher O_2-removal rate of 0.16 $mL{\cdot}cm^{-2}{\cdot}min^{-1}$, significantly exceeding the 35 $mL{\cdot}g_{(active\ material)}^{-1}$ and 0.02 $mL{\cdot}cm^{-2}{\cdot}min^{-1}$ for commercial absorber (Fig. 3(h)). The above results suggest that the developed EOR controller offers excellent O_2 removal performance.

Traditional equipment used to regulate low O_2 concentration faces challenges including large price and bulky size for N_2 flushing devices, or uncontrollable and low efficient of O_2 removal for commercial O_2 absorbers. In contrast, the EOR controller based on electrochemical mechanism provides an effective solution, being lightweight and compact, and more importantly, enabling multi-dimensional control of the O_2 removal process. This can be achieved by incorporating basic electronic control components into the EOR controller (Fig. 4(a)). Installing a switch between the anode and cathode of the EOR enables real-time control over the activation and deactivation of the reaction. Figure 4(b) indicates that the EOR controller enables convenient activation or shutdown of the O_2 removal function, supporting targeted or segmented adjustments of O_2 concentrations. Moreover, the EOR controller maintains a constant environmental O_2 concentration when shut off, indicating no self-discharging behavior. For study objects that are sensitive to environmental changes, controlling the O_2 removal rate via the EOR is of great importance, as an excessively rapid O_2 removal rate can trigger stress responses in these organisms. The introduction of fixed resistors with varying resistances enables the regulation of the current magnitudes of the EOR controller, thereby controlling the O_2 removal rates. Experimental results (Fig. 4(c)) indicate that introducing 0.5 and 1 Ω resistors into the EOR system decreases the O_2 removal rate as resistance increases. Furthermore, standard linear relationships between O_2 concentrations and times were observed for the EOR controllers incorporating resistances of 0, 0.5, and 1 Ω, suggesting that they all maintain stable discharge currents. Another extraordinary advantage of the EOR controller lies in integrating an O_2 concentration estimation function. This is grounded in the electrochemical reaction principle where the total

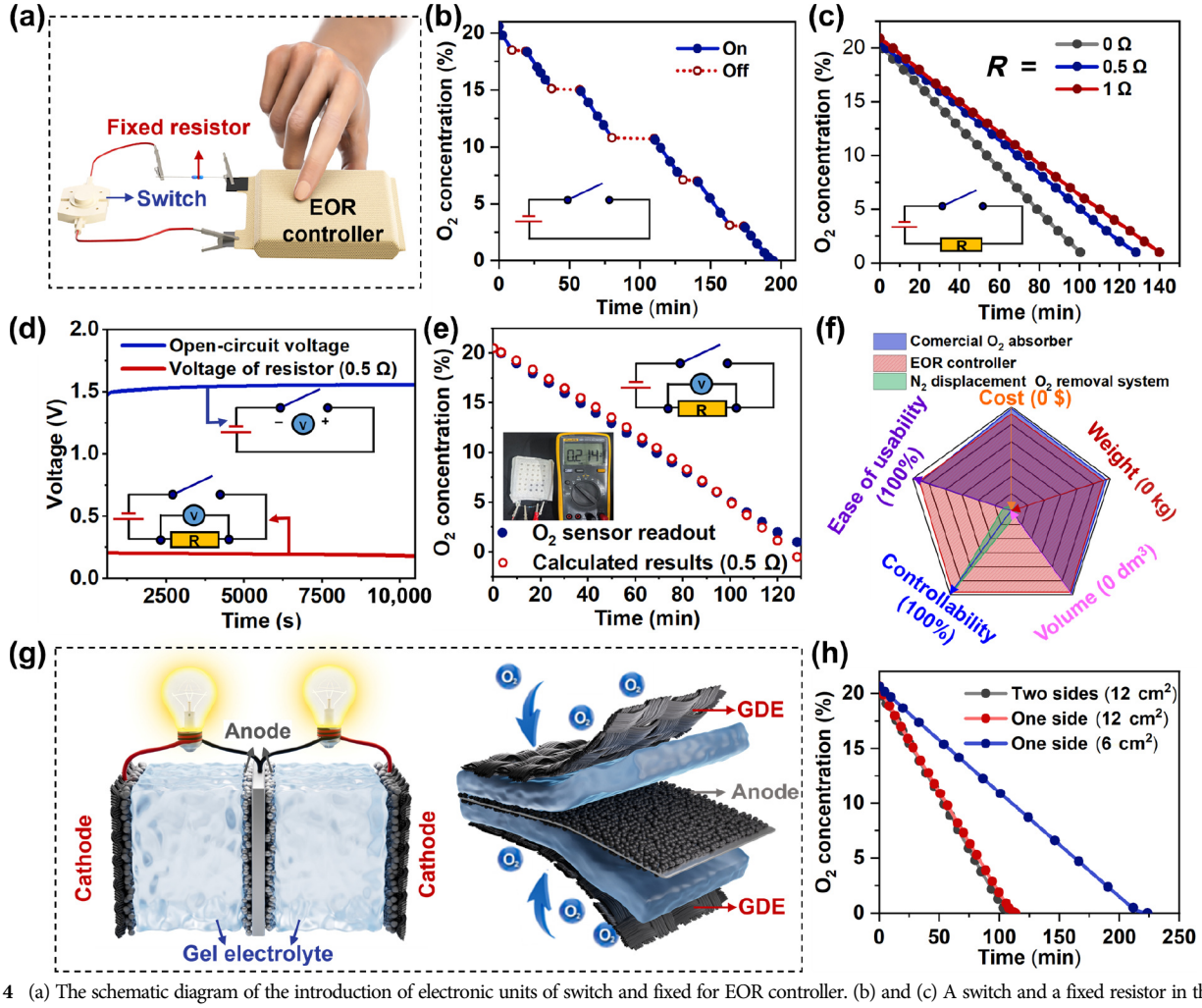

Figure 4 (a) The schematic diagram of the introduction of electronic units of switch and fixed for EOR controller. (b) and (c) A switch and a fixed resistor in the EOR controller are used to enable on–off control and rate adjustment functions during the O_2 removal process. (d) Stability tests of the EOR controller were conducted for the open-circuit voltage and the voltage across the fixed resistor under working conditions. (e) The O_2 concentration results obtained from the O_2 sensor readouts and the electrochemical calculations during the same O_2 removal period. (f) The five-star performance comparison chart for different O_2 removal devices. (g) The mechanism and flexible structure diagram of the double-sided EOR controller. (h) The comparison of double-sided and single-sided EOR in O_2 removal rates.

electron transfer amount determines the amount of reactants consumed. By measuring the discharge current of the EOR controller and the O_2 removal time, the O_2 concentration within a closed system can be directly estimated using an equation derived from Faraday's law. Figure 4(d) revealed a steady open circuit potential for the EOR controller, representing the high stability of the system. The voltage of a 0.5 Ω fixed resistor in a connected system was measured to be stable within 10,000 s under a working condition, indicating a steady discharge current during the overall O_2 removal period. For procedures for estimating environmental O_2 concentrations using EOR controller, a fixed resistor (e.g. 0.5 Ω) was connected to the system circuit in series, and the precise discharge current can be calculated by measuring voltage and dividing by the resistance. Then, counting the O_2 removal time, and estimating the environmental O_2 concentration by the derived equation. To validate the accuracy of the O_2 concentration estimation method, we compared the calculated O_2 concentrations with the real-time readouts of O_2 concentration sensor, and the results are shown in Fig. 4(e) and Video S1 in the ESM. Within the range of 21% to 3%, the estimated O_2 concentrations deviate by less than 0.5% from the O_2 concentration sensor readouts. For the lower O_2 concentration range within 3% to 1%, the accuracy is mildly affected by the restricted O_2 mass transfer, leading to a slightly reduced discharge current of the EOR controller; however, the deviation still remains less than 1%. The above results manifest that the EOR controller may also integrate the function of the O_2 concentration sensor, acquiring relatively accurate O_2 concentrations while removing O_2. This ability is especially beneficial for some application cases that require multiple control experiments, substantially reducing study costs by eliminating the requirement for several O_2 concentration sensors. The performance parameters including function, size, weight, and cost for different O_2 removal devices were summarized and compared in Table S4 in the ESM and the five-star chart Fig. 4(f). Among them, the EOR controller presents remarkable functional cost performance, integrating all functions of O_2 removal, O_2 control, and O_2 concentration estimation into one while still maintaining high miniaturization and an ultra-low cost. Further structural improvements to the EOR controller were made to significantly enhance its O_2 removal rate. This is achieved by designing a parallel connected structure for the EOR controller, which consumes O_2 on both the front and back sides of the device simultaneously, thereby accelerating the O_2 removal process. Figure 4(g) shows the diagrams of working and structure mechanism for a double-sided EOR controller. The EOR controller is assembled with gel diaphragms and GDEs loaded with ORR catalyst on both sides, centered around the anode current collector with Zn powder on either side, thus achieving a parallel connection of two devices. Such a design maintains a small volume and saves material costs as much as possible for the EOR controller, while effectively increasing the O_2 removal rate. The O_2 removal rate of the double-sided EOR controller is compared with that of single-sided EOR controllers, and the results are shown in Fig. 4(h). Compared to a single-sided EOR with a reaction area of 6 cm^2, the double-sided EOR controller, which has a total reaction area of 12 cm^2, exactly doubles the O_2 removal rate. This O_2 removal rate is similar to that of a single-sided EOR with a reaction area of 12 cm^2, demonstrating that the designed parallel structure does not compromise the O_2 removal performance.

To validate the practicality of the EOR controller, several experiments were conducted to simulate hypoxia stress in *Arabidopsis* seeds and seedlings. When environmental O_2 level declines, plants sense oxygen molecules through the N-end rule pathway [29]. In *Arabidopsis thaliana*, when deficient to O_2, transcription factors ethylene response factor VIIs (ERFVIIs) including related to AP2.2 (RAP2.2), related to AP2.3 (RAP2.3), related to AP2.12 (RAP2.12), hypoxia responsive ERF 1 (HRE1) and hypoxia responsive ERF 2 (HRE2) rapidly accumulate and localize to the nucleus, initiating downstream adaptive responses [29]. Studying how plants respond to hypoxic stress at physiological and molecular levels is essential for breeding crops that are tolerant to low O_2 conditions. The EOR controller integrated with a switch and a 0.5 Ω fixed resistor, was introduced into an airtight bag to reduce the ambient O_2 to different target levels, as shown in the experimental photos in Fig. 5(a). The O_2 concentration was directly estimated in real time through the measured discharge current of the EOR system. Observation was made with confocal microscope. As shown in Fig. 5(b), under normoxic condition (21% O_2), 2.3-GFP hardly accumulated and translocated. however, when O_2 concentration decreased to 10%, partial 2.3-GFP were accumulated and translocated, and more accumulation and nuclear localization were observed under 0% O_2. These results prove that the EOR system is effective for controlling O_2 levels in broad O_2 range. In the absence of O_2 concentration sensor, O_2 concentration was further regulated to 5%, 3%, 0% by EOR controller, and anoxic stress test was carried out on seed germination. Figures 5(c) and 5(d) present the results of *Arabidopsis* seeds germination under different O_2 levels. At the atmospheric concentration of 21%, seed germination rate was 98%. However, although the oxygen concentrations of 5%, 3% and 0% were similar, the germination rates were 73%, 17% and 0%, respectively, with significant differences. In terms of seedling growth (Fig. S21 in the ESM), prolonged cultivation of *Arabidopsis* under anoxic conditions leads to chlorosis of leaves. Treatment with the EOR device effectively reproduced this phenotype, demonstrating its utility for observing plant phenotypes under anoxia stress. These results indicate that the developed EOR controller provides effective O_2 concentration control for plant experiments, proving its effectiveness in real-world applications.

4 Conclusion

The study presents an innovative, self-powered EOR controller that significantly simplifies and enhances the efficiency and control of O_2 removal. This EOR controller employs a single-atom ORR catalyst and a flexible structure to substantially reduce both cost and weight. The integration of electronic control elements enables multi-dimensional regulation of the O_2 removal process. In addition, the EOR controller may serve a dual purpose, functioning both as an efficient O_2 removal device and as a O_2 concentration calculator, highlighting its cost performance. Validated through plant hypoxia experiments, it has demonstrated its effectiveness in real-world research applications, offering a reliable and economical solution for O_2 control. This expands the potential of electrochemical technology in environmental gas modulation.

Electronic Supplementary Material: Supplementary material (EXAFS fitting parameters at the Fe K-edge for various samples, device photographs, and XPS characterization) is available in the

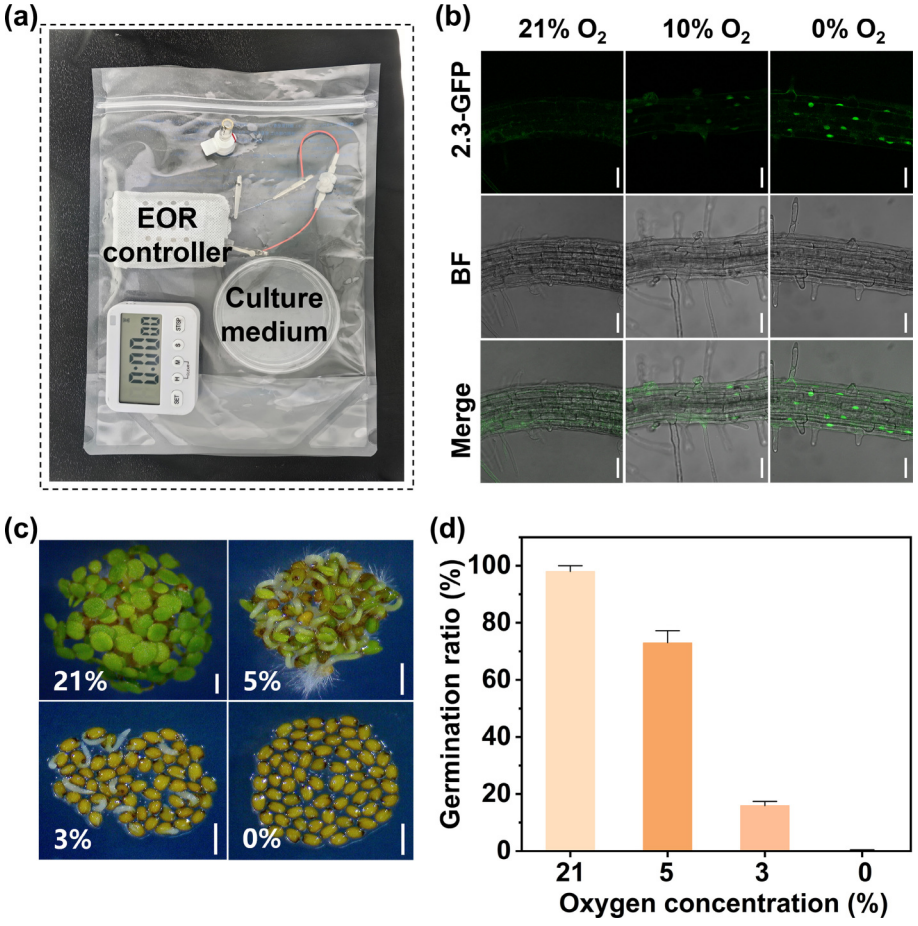

Figure 5 (a) Hypoxic treatments to plants controlled by EOR controller. (b) confocal microscopic experiments to monitor the accumulation and nuclear localization of 2.3-GFP; BF: bright field; merge: 2.3-GFP + BF. (c) and (d) The seed germination assay (c) and germination ratio statistics (d). The tested O_2 concentrations were 0%, 3%, 5%, and 21%, with corresponding seed germination rates measured for each condition.

online version of this article at https://doi.org/10.26599/NR.2025.94907179.

Data availability

All data needed to support the conclusions in the paper are presented in the Electronic Supplementary Material. Additional data related to this paper may be requested from the corresponding author upon request.

Acknowledgements

This work was supported by China Ministry of Science and Technology (No. 2021YFA1600800), the National Natural Science Foundation of China (Nos. 92261105, 22221003, and 22401194), the Joint Funds of the National Natural Science Foundation of China (No. U23A2081), China Postdoctoral Science Foundation funded project (No. 2022M712178), the Anhui Provincial Natural Science Foundation (Nos. 2108085UD06 and 2208085UD04), the Anhui Provincial Key Research and Development Project (Nos. 2023z04020010 and 2022a05020053), the Fundamental Research Funds for the Centre Universities (No. WK9990000155), the Joint Funds from Hefei National Synchrotron Radiation Laboratory (Nos. KY2060000180 and KY2060000195), and the USTC Research Funds of the Double First-Class Initiative (No. YD2060006005). We thank the photoemission endstations BL1W1B in BSRF, BL14W1 in Shanghai Synchrotron Radiation Facility (SSRF), BL10B and BL11U in National Synchrotron Radiation Laboratory (NSRL) for the help in characterizations. We acknowledge Professor Shi Xiao from Sun Yat-sen University for sharing the 2.3-GFP line.

Declaration of competing interest

All the contributing authors report no conflict of interests in this work.

Author contribution statement

Y. E. W., Y. Z., K. C., and S. G. conceived and designed the experiments. X. W. performed the experiments, writing manuscript. X. E. L., W. Y. S., Y. M. L., Y. T., Z. H. W., and P. J. analyzed the data. All the authors have approved the final manuscript.

Use of AI statement

None.

References

[1] Gibbs, D. J.; Lee, S. C.; Isa, N. M.; Gramuglia, S.; Fukao, T.; Bassel, G. W.; Correia, C. S.; Corbineau, F.; Theodoulou, F. L.; Bailey-

Serres, J. et al. Homeostatic response to hypoxia is regulated by the N-end rule pathway in plants. *Nature* **2011**, *479*, 415–418.
[2] Singleton, D. C.; Macann, A.; Wilson, W. R. Therapeutic targeting of the hypoxic tumour microenvironment. *Nat. Rev. Clin. Oncol.* **2021**, *18*, 751–772.
[3] Lu, Z.; Imlay, J. A. When anaerobes encounter oxygen: Mechanisms of oxygen toxicity, tolerance and defence. *Nat. Rev. Microbiol.* **2021**, *19*, 774–785.
[4] Priyadarshi, R.; Jayakumar, A.; de Souza, C. K.; Rhim, J. W.; Kim, J. T. Advances in strawberry postharvest preservation and packaging: A comprehensive review. *Compr. Rev. Food Sci. Food Saf.* **2024**, *23*, e13417.
[5] Kumar, B.; Adebayo, A. K.; Prasad, M.; Capitano, M. L.; Wang, R. Z.; Bhat-Nakshatri, P.; Anjanappa, M.; Simpson, E.; Chen, D. J.; Liu, Y. L. et al. Tumor collection/processing under physioxia uncovers highly relevant signaling networks and drug sensitivity. *Sci. Adv.* **2022**, *8*, eabh3375.
[6] Wang, S.; Yao, S. Q.; Pei, N.; Bai, L. G.; Hao, Z. Y.; Li, D. C.; He, J. K.; Oliveira, J. M.; Xue, X. Y.; Wang, L. et al. Oxygen tension modulates cell function in an *in vitro* three-dimensional glioblastoma tumor model. *Bio-Des. Manuf.* **2024**, *7*, 307–319.
[7] Zhou, Y.; Zhou, D. M.; Yu, W. W.; Shi, L. L.; Zhang, Y.; Lai, Y. X.; Huang, L. P.; Qi, H.; Chen, Q. F.; Yao, N. et al. Phosphatidic acid modulates MPK3- and MPK6-mediated hypoxia signaling in Arabidopsis. *Plant Cell* **2022**, *34*, 889–909.
[8] Koo, D.; Lee, H. G.; Bae, S. H.; Lee, K.; Seo, P. J. Callus proliferation-induced hypoxic microenvironment decreases shoot regeneration competence in *Arabidopsis*. *Mol. Plant* **2024**, *17*, 395–408.
[9] Nagai, K.; Mori, Y.; Ishikawa, S.; Furuta, T.; Gamuyao, R.; Niimi, Y.; Hobo, T.; Fukuda, M.; Kojima, M.; Takebayashi, Y. et al. Antagonistic regulation of the gibberellic acid response during stem growth in rice. *Nature* **2020**, *584*, 109–114.
[10] Quaglieri, C.; Jourdes, M.; Waffo-Teguo, P.; Teissedre, P. L. Updated knowledge about pyranoanthocyanins: Impact of oxygen on their contents, and contribution in the winemaking process to overall wine color. *Trends Food Sci Technol* **2017**, *67*, 139–149.
[11] Sołowski, G.; Konkol, I.; Cenian, A. Methane and hydrogen production from cotton waste by dark fermentation under anaerobic and micro-aerobic conditions. *Biomass Bioenergy* **2020**, *138*, 105576.
[12] Mesquita, T. J. B.; Sargo, C. R.; Fuzer Neto, J. R.; Paredes, S. A. H.; de campos Giordano, R.; Horta, A. C. L.; Zangirolami, T. C. Metabolic fluxes-oriented control of bioreactors: A novel approach to tune micro-aeration and substrate feeding in fermentations. *Microb. Cell Fact.* **2019**, *18*, 150.
[13] Enomoto, T.; Tokizawa, M.; Ito, H.; Iuchi, S.; Kobayashi, M.; Yamamoto, Y. Y.; Kobayashi, Y.; Koyama, H. STOP1 regulates the expression of *HsfA2* and *GDHs* that are critical for low-oxygen tolerance in Arabidopsis. *J. Exp. Bot.* **2019**, *70*, 3297–3311.
[14] Dey, A.; Neogi, S. Oxygen scavengers for food packaging applications: A review. *Trends Food Sci. Technol.* **2019**, *90*, 26–34.
[15] Mathew, I. E.; Rhein, H. S.; Green, A. J.; Hirschi, K. D. Generating reproducing anoxia conditions for plant phenotyping. *Bio-protocol* **2023**, *13*, e4603.
[16] Shao, W. J.; Yan, R.; Zhou, M.; Ma, L.; Roth, C.; Ma, T.; Cao, S. J.; Cheng, C.; Yin, B.; Li, S. Carbon-based electrodes for advanced zinc-air batteries: Oxygen-catalytic site regulation and nanostructure design. *Electrochem. Energy Rev.* **2023**, *6*, 11.
[17] Zhao, Y. G.; Adiyeri Saseendran, D. P.; Huang, C.; Triana, C. A.; Marks, W. R.; Chen, H.; Zhao, H.; Patzke, G. R. Oxygen evolution/reduction reaction catalysts: From *in situ* monitoring and reaction mechanisms to rational design. *Chem. Rev.* **2023**, *123*, 6257–6358.
[18] Jiao, C. L.; Xu, Z. A.; Shao, J. Z.; Xia, Y.; Tseng, J.; Ren, G. Y.; Zhang, N. J.; Liu, P. F.; Liu, C. X.; Li, G. S. et al. High-density atomic Fe–N_4/C in tubular, biomass-derived, nitrogen-rich porous carbon as air-electrodes for flexible Zn-air batteries. *Adv. Funct. Mater.* **2023**, *33*, 2213897.
[19] Jiao, Y.; Zheng, Y.; Jaroniec, M.; Qiao, S. Z. Origin of the electrocatalytic oxygen reduction activity of graphene-based catalysts: A roadmap to achieve the best performance. *J. Am. Chem. Soc.* **2014**, *136*, 4394–4403.
[20] Zhao, X. Y.; Zhao, J.; Li, D. M.; Zhou, F. Y.; Li, P.; Tan, Y.; Zhou, H.; Zhang, Y.; Lin, S.; Wu, Y. E. Electrolyte-free electrochemical oxygen generator for providing sterile and medical-grade oxygen in household applications. *Device* **2024**, *2*, 100360.
[21] Zhang, Y.; Xie, K.; Zhou, F. Y.; Wang, F. T.; Xu, Q.; Hu, J.; Ding, H. H.; Li, P.; Tan, Y.; Li, D. M. et al. Electrochemical oxygen generator with 99.9% oxygen purity and high energy efficiency. *Adv. Energy Mater.* **2022**, *12*, 2201027.
[22] Wang, Y.; Ma, F. Y.; Zhang, G. Q.; Zhang, J. W.; Zhao, H.; Dong, Y. M.; Wang, D. S. Precise synthesis of dual atom sites for electrocatalysis. *Nano Res.* **2024**, *17*, 9397–9427.
[23] Wang, L. G.; Wu, J. B.; Wang, S. W.; Liu, H.; Wang, Y.; Wang, D. S. The reformation of catalyst: From a trial-and-error synthesis to rational design. *Nano Res.* **2024**, *17*, 3261–3301.
[24] Mu, X. Q.; Liu, S. L.; Zhang, M. Y.; Zhuang, Z. C.; Chen, D.; Liao, Y. R.; Zhao, H. Y.; Mu, S. C.; Wang, D. S.; Dai, Z. H. Symmetry-broken Ru nanoparticles with parasitic Ru–Co dual-single atoms overcome the volmer step of alkaline hydrogen oxidation. *Angew. Chem., Int. Ed.* **2024**, *63*, e202319618.
[25] Guo, Y. J.; Liu, Z. Y.; Zhou, D. Y.; Zhang, M. Y.; Zhang, Y.; Li, R. Z.; Liu, S. L.; Wang, D. S.; Dai, Z. H. Competition and synergistic effects of Ru-based single-atom and cluster catalysts in electrocatalytic reactions. *Sci. China Mater.* **2024**, *67*, 1706–1720.
[26] Gao, Y.; Wang, D. S. Atomically dispersed catalysts: Precise synthesis, structural regulation, and structure–activity relationship. *CCS Chem.* **2024**, *6*, 833–855.
[27] Chen, K.; Gao, J. H.; Sun, S. J.; Zhang, Z. J.; Yu, B.; Li, J.; Xie, C. G.; Li, G. J.; Wang, P. C.; Song, C. P. et al. BONZAI proteins control global osmotic stress responses in plants. *Curr. Biol.* **2020**, *30*, 4815–4825.e4.
[28] Wang, Q. C.; Kaushik, S.; Xiao, X.; Xu, Q. Sustainable zinc-air battery chemistry: Advances, challenges and prospects. *Chem. Soc. Rev.* **2023**, *52*, 6139–6190.
[29] Zhou, Y.; Tan, W. J.; Xie, L. J.; Qi, H.; Yang, Y. C.; Huang, L. P.; Lai, Y. X.; Tan, Y. F.; Zhou, D. M.; Yu, L. J. et al. Polyunsaturated linolenoyl-CoA modulates ERF-VII-mediated hypoxia signaling in *Arabidopsis*. *J. Integr. Plant Biol.* **2020**, *62*, 330–348.